Beam-loss detection for the high-rate superconducting upgrade to the SLAC Linac Coherent Light Source

Alan S. Fisher,* Christine I. Clarke, Bryce T. Jacobson, Ruslan Kadyrov, Evan Rodriguez, Mario Santana Leitner, Leonid Sapozhnikov, and James J. Welch

SLAC National Accelerator Laboratory, Menlo Park, California 94025, USA

(Received 18 March 2020; accepted 16 July 2020; published 14 August 2020)

The Linac Coherent Light Source (LCLS) x-ray free-electron laser is driven by the third kilometer of the 3-km SLAC linac, which accelerates electrons in normal-conducting copper cavities pulsed at 120 Hz. The first kilometer is being replaced by LCLS-II, a superconducting (SC) electron linac driven by continuous rf at 1.3 GHz and with a normal-conducting photocathode gun using continuous rf at a subharmonic, 186 MHz. Its 4-GeV, 120-kW beam has a 1-MHz maximum rate, with an upgrade to 8 GeV in planning. The beam from either linac can be switched pulse by pulse to either of two new undulators, to generate hard and soft x rays. Control of beam loss is critical for machine and personnel safety. Previous SLAC protection systems have depended on ionization chambers, including both local devices at expected loss sites and long gas-dielectric coaxial cables providing distributed coverage. These devices are unsuited to the SC-linac beam, because their ion collection time, over 1 ms, may allow the space charge of accumulated ions to null the electric field inside the detector, blinding it to an increase in loss. Instead, both the local and the distributed detectors have been replaced with faster devices. The full 4 km will be spanned by multiple radiation-hard optical fibers in lengths of up to 200 m, each coupled to a photomultiplier tube, to capture Cherenkov light from loss showers. These are supplemented by single-crystal diamond detectors at expected loss sites. Signals are integrated with a 500-ms time constant; the beam is stopped within 200 μs if a threshold is exceeded. We report on our extensive tests of the detectors and the new signal processing.

DOI: 10.1103/PhysRevAccelBeams.23.082802

I. INTRODUCTION

The Linac Coherent Light Source (LCLS) x-ray free-electron laser (FEL) at SLAC National Accelerator Laboratory began operation in 2009 [1] using the third kilometer of SLAC's 3-km linear accelerator (Fig. 1). It retained the 2856-MHz normal-conducting (NC) copper linac used in all projects since 1966 but added a 1.6-cell copper radio-frequency (rf) photocathode gun at 2856 MHz and two bunch-compression chicanes. Both the gun and the linac are pulsed at 120 Hz.

For the LCLS-II project [2], SLAC has removed the first kilometer of the linac, completely emptying this part of the tunnel and the klystron gallery above it for the first time since construction. Cryomodules for a new superconducting (SC) linac are being installed to replace the copper structures. Commissioning is planned for 2021. In addition, two variable-gap undulators, for hard and soft x rays (Fig. 1), have replaced the fixed-gap undulator used for the past decade. Kickers will direct beams from either linac into either undulator, or into a dump upstream, providing users with full flexibility in the x-ray energy and rate.

FACET-II, a user facility mainly for advanced acceleration studies [3], will occupy the middle kilometer with a copper linac and rf photocathode gun, both pulsed at 30 Hz. The beam from the LCLS SC linac will bypass both FACET-II and the LCLS NC linac in a transport line suspended from the tunnel ceiling, only 125 cm from the two linacs below.

Table I compares some parameters of the superconducting and copper linacs. The SC linac, driven with continuous-wave (cw) 1.3-GHz rf, accelerates electrons to 4 GeV. Its normal-conducting photocathode gun is driven by cw rf at the seventh subharmonic (185.7 MHz) of the linac frequency. The pulse rate, set by the photocathode laser, is variable up to 1 MHz. The new machine raises the maximum beam power from 450 W to 120 kW. A planned high-energy (HE) upgrade to 8 GeV will later triple this power.

A. Controls to limit beam loss

SLAC has multiple control systems that limit beam loss, structured in three tiers. The highest is the personnel

*Corresponding author.
afisher@slac.stanford.edu

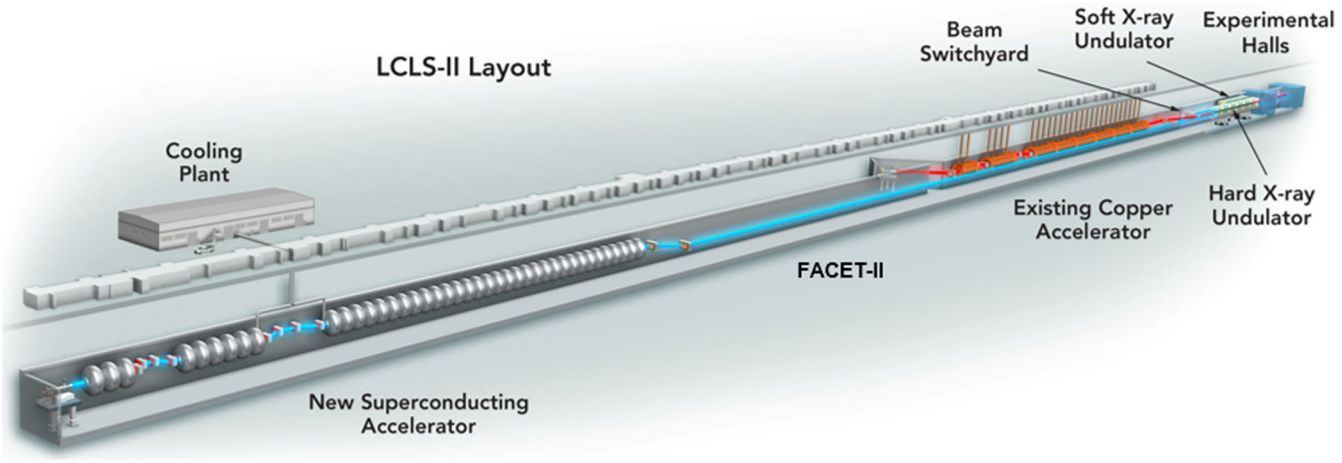

FIG. 1. Layout of the LCLS-II project, showing the new superconducting linac at left. Its beam passes over FACET-II and the original LCLS, both normal-conducting copper linacs. Bunches from either LCLS source can be kicked into either of the two new undulators, for hard and soft x rays.

protection system (PPS), which is a radiation safety system that interlocks access to the accelerator housing and stops the beam if radiation is found in occupied areas. PPS instrumentation will not be further discussed here.

The next tier is the beam containment system (BCS), which is also a radiation safety system and constitutes the main focus of this work. The BCS "trips" (stops) the beam if radiation from the beam or the loss of beam current indicates possible harm to people or to safety devices like protection collimators. It requires robust and simple signal processing, with no knowledge of bunch timing. As safety systems, both PPS and BCS have rigorous configuration control.

The machine protection system (MPS) is allowed greater flexibility to avoid damage from losses. It can trip the beam or reduce its repetition rate if losses exceed a threshold. Insertion of an obstacle such as a valve requires a trip, but insertion of a screen to view the beam requires only a low beam rate. An excessive temperature may be addressed with a rate limit as well. These limits can be imposed by controlling the rate of the photocathode laser. The MPS can selectively block one beam path (such as the beam line for one undulator) while permitting the beam elsewhere by removing the permit for the kicker for that beam line. These remedies can be easily reversed after adjustments are made. Since recovery from an MPS trip is much faster than from a BCS trip, MPS thresholds are set typically 10 times below BCS, so that the MPS trips before the BCS thresholds are exceeded.

B. Beam-loss detection

Both the BCS and MPS detect losses by placing radiation sensors at points of concern along the beam path, often with some redundancy. To trip on losses from both photocurrent and dark current, at any beam rate, the charge collected by a loss detector is passively integrated on a capacitor. Once this capacitor voltage crosses a threshold, a trip command is issued. The choice and location of these sensors will be discussed in detail below.

In previous installations, the BCS and MPS have separate detectors and signal processing. To avoid this duplication, the new beam-loss detectors will serve three purposes: BCS, MPS, and beam diagnostics. Losses below the trip thresholds will provide diagnostic information to operators for tuning the machine and locating high-loss points to avoid or recover from a rate limit or trip. Detector

TABLE I. Parameters of the LCLS NC and SC linacs, as well as the planned HE upgrade of the SC linac.

Parameter	LCLS	LCLS-II	LCLS-II HE
Electron energy (GeV)	≤15	4	8
Bunch charge (pC)	20–300	20–300	20–300
Allowed beam power (kW)	0.45	120	360
Gun frequency (MHz)	2856	185.7	185.7
Linac frequency (MHz)	2856	1300	1300
rf pulse rate (Hz)	120	Continuous	Continuous
Photoelectron bunch rate	1–120 Hz	1 Hz to 929 kHz	1 Hz to 929 kHz
Photon energy (keV)	0.2–12	0.2–5	≤20

signals will be split outside the tunnel for independent processing for these three applications.

C. Point and long beam-loss monitors

Two detector types measure beam losses. Point beam-loss monitors (PBLMs) set limits at critical loss points, such as collimators, stoppers, and dumps. Each halo collimator includes a PBLM connected to the MPS. A modest level of halo loss is expected, but excessive power may result from incorrect steering of the beam or positioning of a collimator jaw. Other PBLMs measure radiation from protection collimators, for the BCS. These devices normally do not receive a beam. In many locations downstream of the linac tunnel, if a beam passes through the thin beam pipe wall, a protection collimator—a barrier typically 50 cm square and four radiation lengths (73 mm of steel) thick, surrounding the beam pipe—spreads out the beam to prevent a direct hit downstream by a thin beam, especially in certain zones with weak shielding.

Long beam-loss monitors (LBLMs) detect losses over tens to hundreds of meters and can protect the entire beam path, from the electron gun to the beam dump. LBLMs can detect losses at unanticipated spots, where no PBLM was placed, as well as distributed losses. We will see that an LBLM can locate photocurrent loss points within a few meters by the signal's arrival time.

D. Loss thresholds and response times

The substantial increase in beam power with the SC linac is accompanied by a proportionate rise in the risk of beam loss that can endanger personnel or damage the machine, especially since losses can continue indefinitely in linacs. The loss can arrive in a fast burst as the full photocurrent beam is lost, or a steady but smaller loss may arrive over a longer integration time. The repetition rate of the losses can be at any beam rate from 10 Hz to 1 MHz (but a full loss at 1 Hz is permitted for tuning).

Field emission (dark current) from the gun or linac may generate loss in every rf period (Table I) and would appear as a dc signal in the loss detectors. Gun dark current may begin somewhat off orbit, travel through the entire linac, and damage the undulator. Cavity dark current can gain significant energy as it travels through several cryomodules in either direction, depending on the rf phase at emission.

Safety systems for the NC linac have 8.3 ms (a 120-Hz period) between pulses to respond to a loss exceeding an MPS or BCS threshold. The SC linac, running at up to 1 MHz, demands greater speed, both in detecting losses and in responding by halting the beam or limiting its rate. Losses exceeding the MPS or BCS trip thresholds must be detected and mitigated within 200 μs so that a direct impact by the beam does not lead to melting or damaging thermal stress [4]. The MPS can mitigate by lowering the rate, but the BCS must shut the beam off. Losses that accumulate over times longer than 500 ms without crossing the threshold are not considered sufficiently harmful to warrant a trip.

Table II lists the criteria for typical locations. Trip specifications vary with the tunnel depth and other shielding and are given in joules of beam loss within the 500-ms integration time. BCS thresholds range from 17.5 to 500 J. MPS thresholds are generally set 10 times lower.

II. IONIZATION DETECTORS

Two categories of detector monitor beam losses for the BCS and MPS, providing different coverage and some redundancy. PBLMs are placed at likely loss locations such as collimators. LBLMs detect losses over longer distances, at least tens of meters.

At SLAC, these functions have long been based on two types of ionization detector. After describing them, we discuss how slow ion collection would limit their performance at high rates.

A. Protection ion chambers

A protection ionization chamber (PIC) is a PBLM placed near a component such as a collimator, to protect it from damage from a beam strike. Figure 2 sketches the design, a stainless-steel cylinder containing a stack of 32 metal plates biased alternately at ground or (typically) −300 V. At this voltage, collection of electrons from showers of ionizing radiation takes 2 μs, but ions require 1 ms of drift time.

TABLE II. Thresholds and times for the BCS and MPS faults at various locations in LCLS-II.

Location	Integration time (ms)	Trip threshold (J) BCS	MPS
Point beam-loss monitors			
Protection and halo collimators	500	50	5
Beam stops and dumps	500	50	5
Long beam-loss monitors			
Superconducting linac and BSY	500	500	50
Beam-transfer hall (BSY to undulator): fence open	500	2.5	1.25
Beam-transfer hall (BSY to undulator): fence closed	500	17.5	1.75
Beam-dump hall	500	100	10

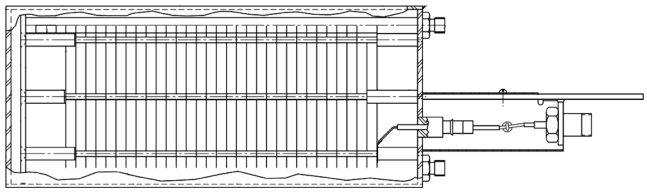

FIG. 2. Cutaway view of a PIC. The housing is a stainless-steel cylinder with a 114-mm outer diameter and a 270-mm length. The 32 plates each have an area of 56.5 cm^2 and are $d = 6.15$ mm apart. The plates are alternately grounded or connected to a bias voltage.

B. Long ionization chambers

A long ionization chamber (LION) [5] detects losses along an extended region of the tunnel. A LION (Fig. 3) is a type of Heliax® coaxial cable with a nominal diameter of 1⅝ inch (41 mm). The corrugated Heliax outer conductor is made with continuous helically wound copper strips. A copper tube forms the inner conductor. The type used for the LION is hollow, with air or another gas serving as the dielectric. Both PICs and LIONs generally operate at a pressure of 125–150 kPa using a mixture of 95% Ar and 5% CO_2. LIONs are typically 30–100 m long and cover selected regions but not the full machine.

A loss shower passes through the cable, ionizing the gas. A typical bias of +250 V on the center conductor drives charge radially, with a collection time of 6 μs for electrons but 6 ms for ions. The charge forms a voltage pulse moving in both directions along the cable. One end leads to a high-voltage supply, an integrator, and a digitizer. The other end has a high-impedance termination drawing a small dc current, called the "pedestal," which indicates that the system is functioning. However, it masks detection of smaller loss currents.

C. 1D model of an ionization chamber

The possible loss of significant beam power and an ion collection time far longer than the interval between pulses both suggest that ion space charge may accumulate inside an ionization chamber. An experimental and numerical study of ionization chambers for protons in the NuMI experiment at Fermilab [6] found that screening by positive ions can completely null the field near the positive electrode(s), creating a "dead zone." This motivated the development of a self-consistent one-dimensional model of charge flow and field evolution in the SLAC devices.

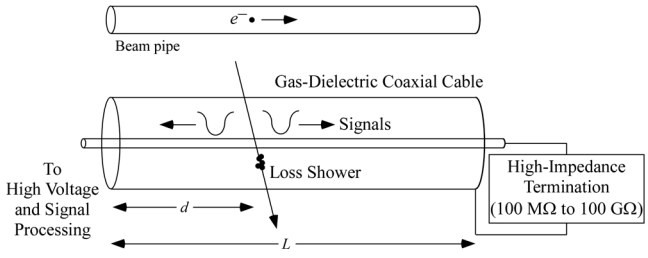

FIG. 3. Sketch of a LION. The nominal inner- and outer-conductor diameters are 18.1 and 46.5 mm, respectively.

The model assumes a uniform ionization rate $I(t)$ per unit volume generated by beam loss and a recombination rate per unit volume $\beta n_i n_e$ proportional to the product of electron and ion densities. The PIC behavior is computed for the x coordinate between a pair of plates. The signal current is then scaled by 31 to account for all plates. The LION model computes the radial behavior per unit length in a uniformly ionized cable.

This numerical model (as well as the experiments discussed later) uses pure argon at a pressure of 100 kPa. Argon, a common gas in ionization chambers, avoids both the complexity of molecular fragmentation and also the creation of negative ions, which move as slowly as positive ions and so would introduce additional space-charge accumulation, in this case near the negative electrode(s).

At this pressure, ions and electrons have mean free paths much smaller than the chamber size, and so particle drift is modeled by an ion mobility μ_i (with a velocity $\mathbf{v_i}$ proportional to the electric field $\mathbf{E}$) and an electron mobility μ_e (which retains a weak E dependence). The ion and electron particle fluxes $\mathbf{J}_{i,e}$ also include a diffusive component with coefficients $D_{i,e}$. Gauss's law gives $\mathbf{E}$ self-consistently. The governing equations in SI units are

$$\begin{aligned} \mathbf{J}_{i,e} &= \pm\mu_{i,e} n_{i,e}\mathbf{E} - D_{i,e}\nabla n_{i,e}, \\ \frac{\partial n_{i,e}}{\partial t} &= -\nabla\cdot\mathbf{J}_{i,e} + I - \beta n_i n_e, \\ \varepsilon\nabla\cdot\mathbf{E} &= e(n_i - n_e). \end{aligned} \tag{1}$$

Here, e is the elementary charge. The effective dielectric ε is ε_0 in a PIC but slightly higher in a LION due to the cable's construction.

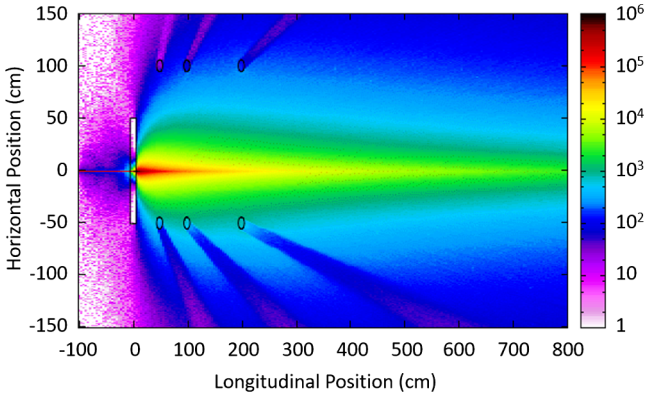

FIG. 4. Model of the radiation field showing a loss on a protection collimator at $z = 0$. The color scale gives the dose in eV/g per incident 4-GeV electron (for which 1 eV/g = 250 nGy/J). Six PICs (with axes perpendicular to the page) are inserted at $z = 50$, 100, and 200 cm and at $r = 50$ and 100 cm. Shielding by their steel housings creates the shadows. The dose at these PICs peaks at 170 and 36 μGy/J at $r = 50$ and 100 cm, respectively, and drops slowly with increasing z.

Electrodes are charge sinks but not sources: Electrons or ions can flow in but not out. The surface charge Q on each electrode is determined self-consistently as an integral over the electrode's surface S. In addition, the bias supply provides the charge required to maintain a constant voltage V_0, given by a line integral $d\mathbf{u}$ between any points a and b on the two electrodes:

$$Q = \varepsilon \int_S \mathbf{E} \cdot d\mathbf{S},$$
$$V_0 = -\int_a^b \mathbf{E} \cdot d\mathbf{u}. \quad (2)$$

A current I_{ext} flows through the external circuit from the bias supply. The current I_S changing the surface charge is the sum of I_{ext} and the collection of electrons or ions:

$$I_S = I_{\text{ext}} \pm e \int_S \mathbf{J}_{i,e} \cdot d\mathbf{S}. \quad (3)$$

D. Loss on a protection collimator

To complete the model, consider a typical loss point, a protection collimator. These are mostly found in the beam-transfer hall (BTH), between the beam switchyard (BSY) and the undulator hall. Because of the hilly terrain, the BTH lies at ground level and is shielded within a concrete bunker designed for the far lower beam power of the NC linac. Additional measures, including low BCS and MPS thresholds, are needed for protection from the SC linac beam.

Because a high-power beam loss could expose people outside to a harmful radiation dose, the region adjacent to the walls is restricted by an interlocked fence. For further safety, any beam escaping the beam pipe must hit a nearby protection collimator surrounding the beam pipe further downstream. Scattering in the collimator's 73-mm thickness of stainless steel spreads out the radiation shower.

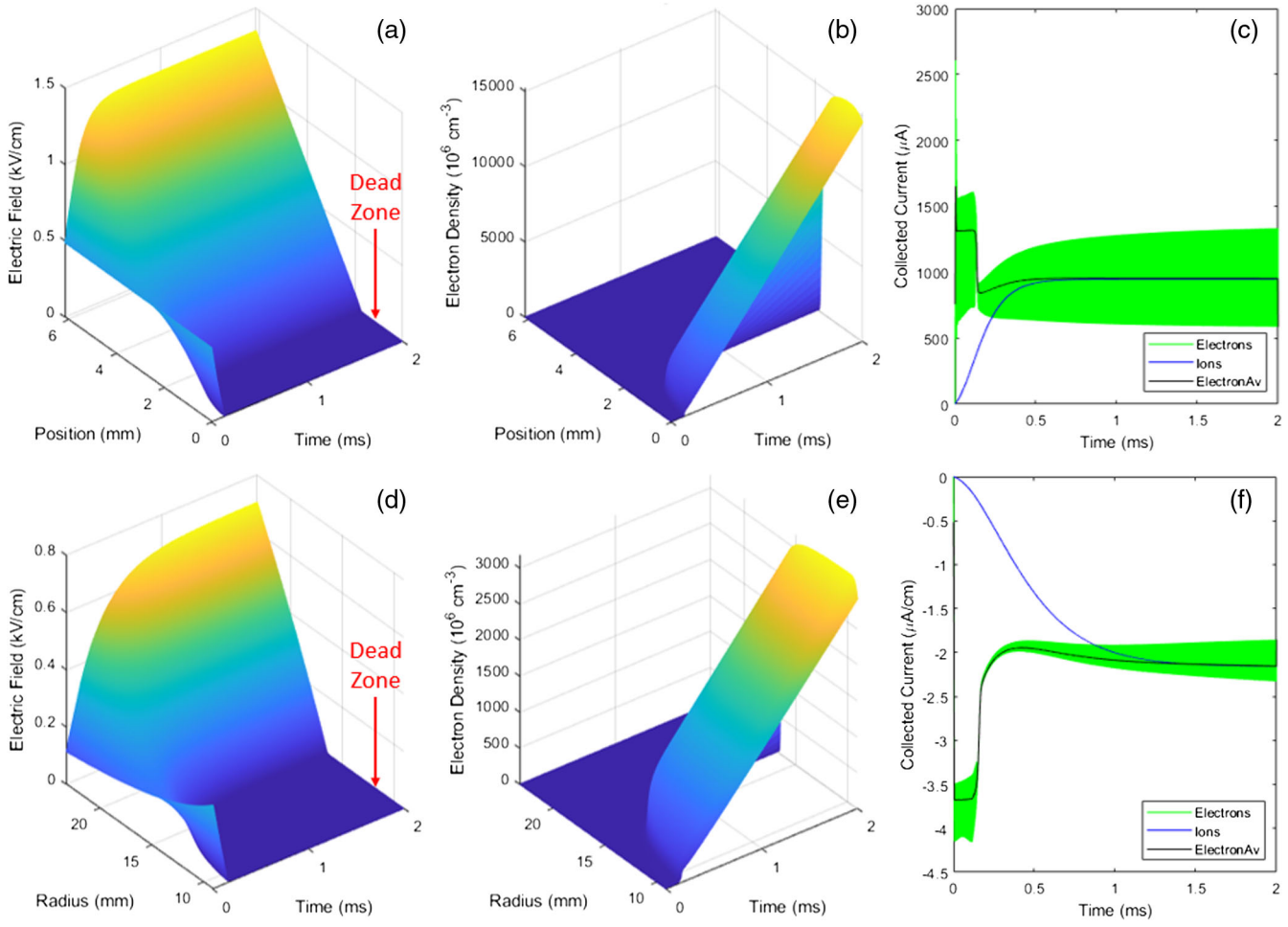

FIG. 5. Response to a 120-kW loss of a 1-MHz beam on a protection collimator over 2 ms. (a)–(c) Response of a PIC placed at $r = 0.5$ m and at the radiation peak in z in Fig. 4, as a function of time and, in (a),(b), of position between adjacent plates. (d)–(f) Response of a LION at $r = 1$ m and spanning the radiation peak, as a function of time and, in (d),(e), of the position between the inner and outer coaxial conductors. (a),(d) Electric field. (b),(e) Electron density. (c),(f) Ion and electron currents collected at the cathode and anode, respectively. Because the electron current fluctuates over a wide band during the 1-MHz period, the average current in each period is also shown.

A hollow layer within the collimator is filled with nitrogen above atmospheric pressure. If a beam burns through the steel to this gas pocket, a pressure switch shuts the photocathode laser off.

The FLUKA model in Fig. 4, showing the dose from beam loss at a protection collimator, relates the lost beam energy to the radiation dose nearby [7], as a function of the distance radially (r) and longitudinally (z) from the collimator at $r = z = 0$. By definition, a dose of 1 Gy deposits 1 J/kg, and an energy of 27 eV is needed to create an electron-ion pair in argon. We can then calculate the ionization in a PIC or LION near the collimator.

E. Model results for PICs and LIONs

Figures 5(a)–5(c) show the response of a PIC to a loss of 120 kW—the allowed power in the superconducting beam—on a protection collimator for the first 2 ms after the loss begins. The PIC is placed at $r = 50$ cm and at the z corresponding to the peak of the radiation field in Fig. 4, 170 μGy/J. The BCS loss limit for a protection collimator, 50 J (Table II), results in a dose of 8.5 mGy.

The electric field is shown in Fig. 5(a) as a function of the time and position between adjacent plates. The ground is at $x = 0$, and the standard bias of -300 V is applied to the plate at $x = d$. The field between the parallel plates is initially uniform, and all the field lines terminate on surface charge on the plates. As the ions accumulate faster than they can travel to the negative plate, some field lines from the negative plate terminate on ion space charge before reaching the positive plate; after 160 μs, the field near the positive plate is completely screened. We call the resulting region of zero field the "dead zone." Since the bias supply maintains a constant voltage difference, the field must grow toward the negative plate.

Transport of electrons and ions (except for diffusion) halts in the dead zone, and both the electron [Fig. 5(b)] and ion densities grow quickly there with the periodic (1 MHz) loss. The collected electron current [Fig. 5(c)] shows a highly nonlinear drop. Note that this nonlinearity occurs after 160 μs, a time corresponding to a beam loss of 19 J, less than half of the BCS limit.

A LION receives a dose near the peak value over a length of about 1 m, and so we use 35 μGy/J for $r = 1$ m. In Figs. 5(d)–5(f), the LION exhibits behavior similar to that of the PIC, exacerbated by a larger electrode separation. Again, a dead zone forms, and the electron density rises rapidly there. The collected electron current becomes nonlinear after 125 μs, corresponding again to 15 J of loss. The bias is the standard +250 V, with the ground on the outer conductor. A negative bias would be worse: The $1/r$ dependence of the coaxial field makes it weaker at the outer electrode and so reduces ion transport in this critical region, making the field easier to screen.

We see that both ionization detectors can become nonlinear at loss levels below the BCS thresholds. Such behavior is inappropriate for a critical safety system. Although the MPS is designed to trip at a lower losses, the BCS must work independently. Some improvement could be obtained with greater distance and higher voltage but would not fully address these failings. Also, the gas-distribution system now deployed over the accelerator complex has limitations in reliability, and extending it would be expensive. These considerations led us to investigate other detector types.

III. LBLMS FOR LCLS-II

A. Optical fibers

In place of LIONs, SLAC has selected optical fibers as LBLMs for the LCLS-II project. A loss shower passing through a fiber emits Cherenkov light, a portion of which is captured in a fiber mode and carried to a photomultiplier tube (PMT) at one end. For sensitivity, each fiber is relatively thick —with diameters of 600, 660, and 710 μm for the core, cladding, and buffer, respectively—and is encased in a 2-mm jacket of black polyurethane, for protection and opacity. The fiber, type FBP-600660710 from the Polymicro division of Molex, uses a radiation-resistant quartz for both core and cladding. This and related types were subjected to extensive tests of radiation hardness—up to 12.5 MGy—for use in the end cap of the CMS detector on the LHC at CERN [8–10]. The FBP type was found to be superior, especially for red wavelengths around 700 nm.

A distance of 4 km must be protected, from the gun to the beam dump, in most places using two fibers both for redundancy and also for different viewing angles. This distance is subdivided into lengths of roughly 200 m. Variations occur to span functional sections, such as the injector or the L2 linac between the first and second bunch compressors.

Dividing the fiber in this way offers two benefits. First, attenuation of light in the fiber limits the maximum segment length. Also, by restricting the length and sampling the PMT waveform at a high rate, we gain two diagnostic capabilities. First, a loss point can be localized within 3 m by measuring the arrival time of the loss signal from a photocurrent bunch at the PMT, without ambiguity from pulse pileup. When the PMT is placed at the downstream end of the fiber, for reasons addressed later, losses along a 200-m fiber from one bunch span 330 ns, well under the minimum bunch spacing of 1 μs in the SC linac.

Second, when a wire scanner measures the transverse bunch profile, software extracts the portion of the PMT signal due to beam current intercepted by the wire and correlates it with the wire position to determine the beam size, without the need for a dedicated detector at each wire scanner.

B. Fiber attenuation and PMT selection

If light is strongly attenuated in the fiber, then two equal losses, one occurring at the end of the fiber near the PMT

and one at the distant end, will generate PMT signals of very different amplitudes. If trip thresholds are set based on the stronger loss, unacceptable losses at the distant end may not trip the beam. If the thresholds are based on the attenuated signal, then tolerable losses at the near end may cause unnecessary trips. Our criterion is that these signals must not differ by more than 3 dB (a factor of 2). Then the lowest curve in Fig. 6, which plots the inherent attenuation of a 200-m fiber, restricts the wavelengths to $\lambda \geq 510$ nm; shorter wavelengths have too much loss.

A longer cutoff is needed to account for the increase in attenuation after irradiation over several years of use. Measurements made for CMS provide a fit to radiation-induced attenuation as a function of the dose and wavelength [9] for a similar Polymicro quartz fiber, type FVP. Its attenuation is somewhat higher than that of FBP after extensive neutron and gamma irradiation [10], and so the fit [9] allows a conservative calculation of attenuation in our FBP fiber as a function of the dose.

It is unlikely that the entire fiber would be subjected to high levels of radiation. Instead, Fig. 6 presents a scenario in which the fiber passes a strong loss point, where 10 of its 200 m receive various high doses of radiation over time. Near 700 nm, attenuation remains largely independent of the dose and easily satisfies the 3-dB criterion. Wavelengths can be restricted to this range by covering the PMT window with a long-wave-pass filter with a sharp cutoff. The quantum efficiency (QE) of the PMT photocathode itself blocks even longer wavelengths. The combination effectively acts as a bandpass filter with sharp edges.

We must, of course, allow for the reduction in the total signal due to this rejection of shorter wavelengths, especially since Cherenkov emission, although broadband, has an intensity $dI/dxd\omega$ that is proportional to ω [11] and so appears blue. However, a PMT responds not to the intensity but to the photon flux $dN/dxd\omega$, which is flat with

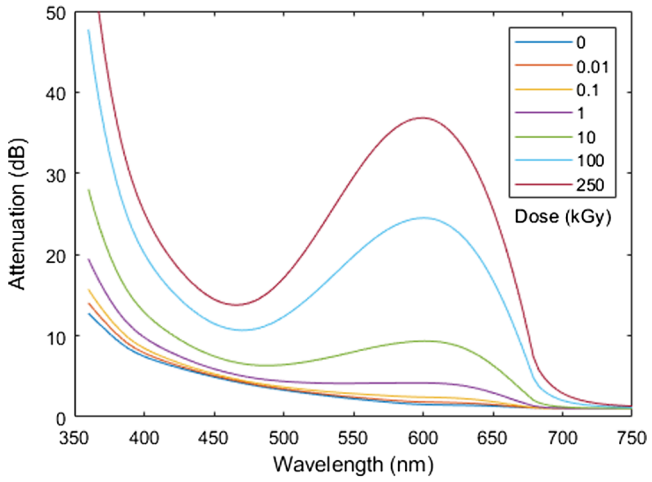

FIG. 6. Radiation-induced attenuation in a 200-m fiber irradiated over 10 m, for various doses in kGy.

frequency (although, expressed in terms of wavelength, $dN/dxd\lambda \sim \lambda^{-2}$). We calculate the relative PMT signal by an integration in wavelength over the product of the Cherenkov emission, the fiber transmission, the color-filter transmission, and the QE of the PMT. Our measurements using the NC linac (presented below) confirm a satisfactory signal in this spectral range near 700 nm.

In an area such as the BTH, the beam must trip at a lower radiation level. If the wavelengths are restricted to the region near 700 nm, the trip threshold would be set at a correspondingly low signal, which could be sensitive to noise. However, since exposure limits require a low radiation dose there, we can afford to raise the signal strength by extending the cutoff wavelength toward the green (but remaining above the zero-dose wavelength limit of 510 nm). A fiber dose limit of 1 kGy in this zone allows several years of use, and calculations based on Fig. 6 find that a cutoff of 555 nm satisfies the 3-dB criterion. In contrast, a fiber in the linac, where the threshold is higher, is also expected to receive a higher dose over a similar time. There, the filter cutoff is 675 nm, allowing a dose of up to 100 kGy.

To verify that a fiber's attenuation has not increased to an unacceptable level, the transmission of each fiber will be continuously monitored with the "heartbeat" introduced in Sec. III C below.

Few photocathode materials are sensitive at wavelengths near 700 nm. The strongest response comes from GaAsP, used in the Hamamatsu H7422P-40 PMT, which has a QE of 30% at this wavelength. However, the low work function needed in any red-sensitive photocathode increases its dark current. This background would mask the detection of structure dark current from an emission site in the electron gun or superconducting rf cavities. Once formed, such a site emits in each rf period, leading to a quasi-cw source of potentially damaging radiation. We calculate that the anode dark current of the PMT should be limited to 1 nA, low for red-sensitive cathodes. However, PMT dark current is thermal, dropping by about a factor of 2 for every 5 °C of cooling until this benefit levels off at 0 °C [12]. The second advantage of the H7422P-40 is the built-in Peltier cooler that maintains an operating temperature of 0 °C.

C. Fiber layout

Both ends of the fiber up come up from the tunnel to the klystron gallery, about 11 m above the tunnel floor. Figure 7 illustrates the layout. One end runs to a rack with an LBLM chassis containing the PMT, with its entrance window covered by a suitable optical filter and an SMA-905 fiber connector.

Figure 7 shows a similar chassis at the other end of the fiber, where it connects to an SMA-905 containing a light-emitting diode (LED) emitting at a wavelength just within the edge of the filter's passband. The LED provides a continuous self-check of the fiber system, called the

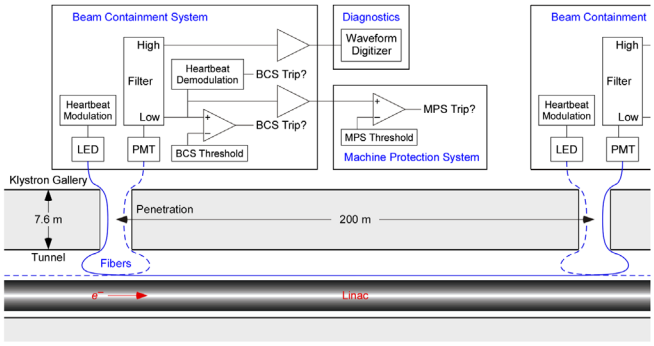

FIG. 7. Typical fiber layout in the linac tunnel, including the PMT at the downstream end and the heartbeat LED at the upstream end. The splitter that provides a signal for three functions is indicated. A solid line indicates the fiber path between the two penetrations shown; the two fibers running beyond this region are shown with dashes.

heartbeat. Its failure trips the BCS. Details are discussed in Sec. V C below.

If a fiber needs replacement after several years, it can be done quickly, without entering the tunnel and without halting the beam. "Ducts" of polyethylene tubing with a 6-mm inner diameter run along the fiber routes. A special tool, aided by the flow of nitrogen at 700 to 1000 kPa, pushes a fiber through a duct. In our tests, a 200-m fiber travels from the rack at one end to the rack at the other end within a few minutes. The fiber is ready for use after SMA connectors are attached to the ends and the tips are polished.

D. Modeling the fibers

The geometry for capturing Cherenkov light in a fiber is complex. This quartz fiber captures only rays traveling within an angle of 8.7° to the axis, allowing them to travel to the PMT. The axis of the Cherenkov cone emitted by a relativistic particle from a loss shower passing through the fiber core lies at 46° to the direction of travel, due to the refractive index of the medium. Only part of the cone can fall within the capture angle. The most effective alignment occurs where the particle's entering angle is close to 45° to the axis, which places the onset just downstream of the loss source. However, showering and screening by intervening objects can alter the signal.

This process has been modeled with a Monte Carlo extension to FLUKA tracing the Cherenkov emission [13]. This simulation finds that 90% of the signal is integrated within 20 m downstream of a thick target (such as a beam stop) and within 50 m from a target of medium thickness, such as a protection collimator. Upstream contributions are minimal. Because the thick target absorbs some of the loss shower, its signal is lower (Fig. 8). The transverse distance d of the fiber from the beam line has a soft effect on the signal, falling off as $d^{-0.79}$ (for d in centimeters).

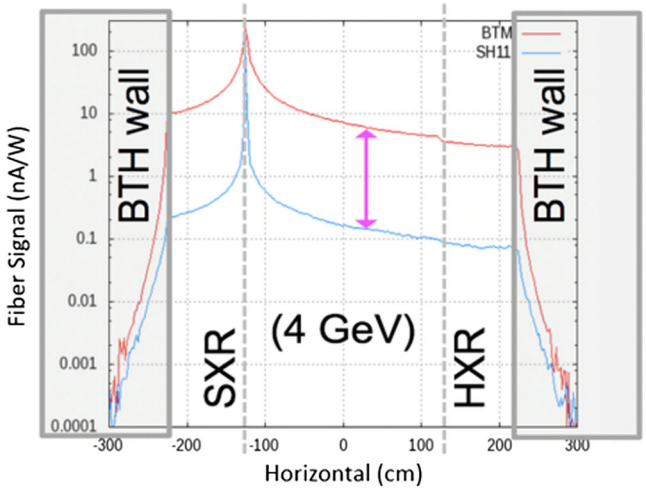

FIG. 8. Simulated signal (nA/W) integrated along the fiber as a function of the horizontal distance to the loss point. The upper trace shows loss on a target of medium thickness (e.g., a protection collimator); the lower traces shows a thick target.

IV. PBLMS FOR LCLS-II

A. Diamond detectors

In place of PICs, the LCLS-II project has selected diamond-based detectors as PBLMs. As a loss shower passes through a thin diamond chip, every 13 eV of lost energy creates an electron-hole pair. A bias voltage between metalized electrodes plated on the opposite faces of the chip separates the pair. The diamond resembles a solid-state ionization chamber but with the important difference that both electrons and holes take only a few nanoseconds to reach the electrodes: No pileup happens at the 1-MHz beam rate. Unlike an LBLM, loss localization through arrival time is not important for a PBLM, since each detector is in a fixed location near expected loss points.

We investigated three types of diamond detectors, all originally developed for CERN and made by Cividec [14]: the single-crystal B1, the polycrystalline B2, and the high-radiation polycrystalline B4. Both the B1 and B2 models have a wide dynamic range, responding to the passage of 1–10^6 minimum ionizing particles (from a loss shower that has cascaded to the minimum of dE/dx). The B2 sensor has the benefit of an active volume that is four times larger than the B1. The B4 is smallest and is designed for a lower sensitivity to avoid saturation in a high-radiation environment. The experiment presented in Sec. VI C found that signals from both polycrystalline types exhibit a slow decay when the loss stopped. The single-crystal B1 shows no such tail and so was chosen for the high repetition rate of the SC linac.

The continuous heartbeat test for the LBLMs was introduced earlier. A similar test was devised for the diamond detectors, accomplished by modulating the bias voltage. Both are detailed in Sec. V C.

B. Modeling the diamonds

Cividec has simulated electron-hole pair production in single-crystal diamond by high-energy electrons, positrons, protons, neutrons, and photons [15]. These results were incorporated into another FLUKA extension [13] that uses the fluences and energies of the various shower particles in a Monte Carlo calculation of the signal from a B1 diamond. Note that the detector's signal depends on its volume ($4 \times 4 \times 0.5$ mm^3 for the B1) but not on its orientation.

The simulations show that this diamond can detect losses on a thick target above 100 mW at a distance of 1 m, below the requirements in Table II. However, the response falls off quickly with distance from such targets. This is an issue with any loss detection in a self-shielding target.

For thinner targets, Fig. 9 shows that the signal from a loss on a protection collimator is nearly constant over a longitudinal distance of as much as 40 m, when measured at a transverse distance of 1.5–2 m from the beam pipe. We see also that the signal from glancing incidence on a beam pipe exceeds that of the protection collimator for distances below 20 m. All the protection collimators in an area can then be covered by locating one diamond every 20 m between beam lines. With many such collimators on adjacent beam lines in the BSY and BTH, this scheme offers a considerable economy in the number of detectors.

In a test of this effect in end station A at SLAC, a beam was incident on a 16-cm-square, 80-mm-thick iron block. A B1 diamond was placed 166 cm to the side, suspended from the shielding wall on a motorized clothesline, and moved downstream of the block from −1 to +17 m. The signal was not flat with distance, as in Fig. 9, but peaked 7 m from the block and dropped by half at 12 m. A more detailed analysis, accounting for the smaller width of the block and screening by obstacles that could not be removed from the tunnel, found consistency with the model.

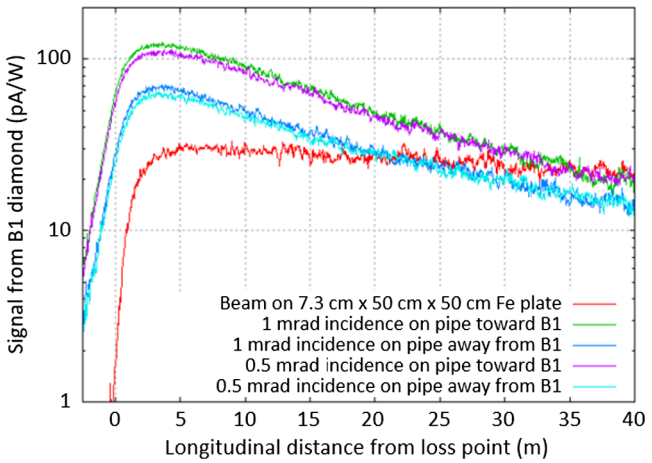

FIG. 9. Simulated current (pA) from a B1 diamond placed 2 m transversely from the beam pipe, as a function of the longitudinal distance from a 1-W beam loss on a protection collimator (red line) or from glancing incidence on a 1.5-mm-thick stainless-steel beam pipe.

C. Scintillators

The cw electron gun for the SC linac has an output energy of 750 keV, low compared to 5 MeV from the pulsed gun of the NC linac. Early commissioning of the gun and the first 3 m of beam line took place over several months in 2019 and again for 3 months in 2020, during installation of linac cryomodules. A temporary Mo cathode was used during initial tests, bakeout, rf processing, and initial observations of dark current. A Cs_2Te photocathode was then installed for photocurrent commissioning.

A short fiber along with two diamonds, one on the exit face of the gun and the other 1 m downstream by the entrance window for photocathode laser light, were installed for injector commissioning. Before electrons accelerate in the first cryomodule, beam loss can generate only a weak response from these detectors, especially the fiber due to the low-energy cutoff of Cherenkov radiation. Consequently, two scintillators of cerium-doped yttrium aluminum perovskite (YAP:Ce, from Crytur) with PMTs were installed next to the diamonds. Dosimeters placed beside these detectors measured the total dose in the 2020 test.

The scintillators easily detected dark current from the Mo photocathode. Adjusting the focusing solenoid at the gun output shifted the loss from one scintillator to the other. During part of the 2020 run, when the gun rf ran for about 4 h per day with dark current only, the second scintillator saturated the electronics (∼10 V, integrated as in Fig. 10 but with a larger C_1). When the rf shut off, the scintillator exhibited a large offset (∼2 V) that decayed slowly with exponential components of 8 and 100 h. The first scintillator reached 5 V with a much smaller offset (∼5 mV) but with the same decay. As expected, the diamond signals were much smaller (a few millivolts) but shut off immediately without offsets or tails. Radiation levels were not unusual for an accelerator: The dosimeters recorded 17 Gy at the second location but only 140 μGy at the first. Because of these tails, the scintillators are not suitable as PBLMs, but the diamonds should prove satisfactory.

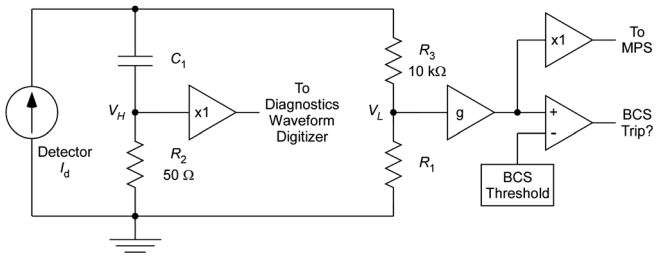

FIG. 10. Front-end circuit showing the input integrator and splitter. The diagnostics waveform is used only with the fiber.

V. SIGNAL PROCESSING

A. Unified design

The requirement for beam-loss detectors suitable for high loss power at high beam rates demands a rapid shutoff, with a time budget of 200 μs from first exceeding the trip threshold to mitigation (by stopping the beam or, for the MPS, possibly lowering the rate). The electronic latency must occupy a small fraction of this interval by responding to a threshold breach within 10 μs. Consequently, a new design was developed for the signal-processing electronics and the overall BCS architecture [16].

Signals from both the LBLMs and PBLMs are integrated over 500 ms. The choice of a negative bias for the diamonds matches their output signal polarity to that of the PMTs. Similar integrated voltage levels can be obtained by selecting suitable components for the charge integrator. Furthermore, both sensors perform a continuous heartbeat self-check (Sec. V C) based on a lock-in algorithm in a digital signal processor (DSP). These commonalities enable a unified front end for the electronics of both sensor types offering significant savings in engineering and design verification.

B. Integrator and splitter

The charge from the diamond sensor or PMT is split into low- and high-frequency components with the passive circuit in Fig. 10. Both sensors are current sources, generating a charge proportional to the loss. The charge is transferred immediately upon arrival to the integration capacitor C_1, which accumulates the charge from a train of loss pulses. A low-leakage film capacitor is used, with a value based on the expected charge at the BCS loss threshold. A capacitance of 33 nF is used for the PBLMs; the LBLMs use 330 nF to 1 μF, depending on the location. For diamonds, C_1 includes the capacitance of the cable from the tunnel. Because each fiber ends at a chassis containing a PMT next to the integration circuit, cable capacitance does not enter into the component values that set the integration time constant.

The capacitor slowly discharges through resistors R_1, R_2, and R_3 in series. A 500-ms time constant is set by R_1, which ranges from 0.5 to 1.5 MΩ for the LBLMs to 15 MΩ for the PBLMs. The integrator output V_L is buffered and scaled by an amplifier with a gain of 2–50, set by switches on the board. The resulting level is compared to the BCS loss threshold. The amplifier needs a low input bias current, to avoid leaking charge from the capacitor, and a low input offset voltage, to avoid affecting the signal on the comparator. Because the klystron gallery is not temperature controlled and the racks are not cooled, the temperature of the electronics can vary diurnally and seasonally from 0 to 50 °C; consequently, the selected amplifier has a low temperature drift to maintain a low offset. The amplified capacitor voltage is buffered by a second amplifier with unity gain before transmission to the MPS digitizer chassis (which in many cases is in another rack).

Each detector has a different threshold, calculated for various loss scenarios. To avoid unintentional changes over the network, the threshold is set locally, with thumbwheel switches on the front panel. Access to this unit is protected with a lock. The threshold level is continuously monitored by a programmable logic controller (PLC), which halts the beam if the value read does not match the expected level.

The high-frequency component V_H of the detector output is terminated in 50 Ω by R_2. For the LBLM, V_H is buffered by a fast amplifier and sent to a 350 MSample/s digitizer. The output waveform provides a diagnostic to locate the beam loss. The arrival time of the loss peak at the digitizer allows us to determine the source of a loss within about 3 m. During a wire scan (Sec. VI E), software extracts

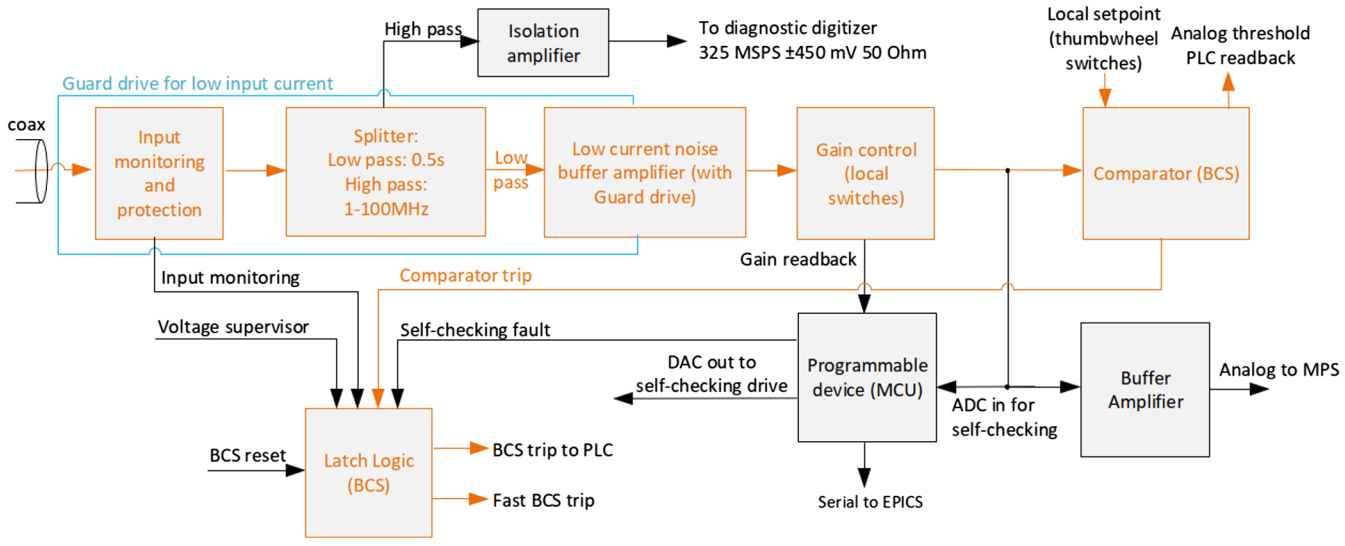

FIG. 11. A functional block diagram of the BLM electronics. Highlighted boxes show the direct path for beam loss.

the portion of the waveform showing the signal from the beam's passage through the wire and correlates it with the wire position to measure the bunch profile projected onto the direction of the wire's motion. The software provides three sampling windows, configurable in width and delay, to numerically integrate loss peaks and subtract pedestal.

Figure 11 shows the various branches and the overall processing scheme. However, it was noted earlier that the PBLM has no need for a fast waveform.

C. Self-checking

We encode the LBLM self-check heartbeat signal by driving a small 0.8-Hz sinusoidal current in the LED at the upstream end of the fiber. A DSP running an algorithm like that of a digital lock-in amplifier sensitively detects this modulation in the PMT output. A missing heartbeat—indicating a failure of the fiber, the PMT, its power supply, or the electronics—trips the BCS. Modulating the current rather than the voltage was found to be more tolerant to LED temperature variations. The control system archives the detected heartbeat amplitude, so that any gradual degradation of the fiber transmission can be tracked.

To create a PBLM heartbeat, its −250-V bias is modulated by 5 V peak to peak. The resulting small current through the diamond capacitance is also detected by a lock-in implemented on a DSP. The modulation varies the few-nanosecond transit time to the electrodes proportionately but with no effect on the total charge collected.

The modulation frequency of 0.8 Hz, used with both detector types, avoids any subharmonic of a beam rate, which might influence the demodulated amplitude. Also, this low frequency passes through the *RC* integration filter. The narrow-band filter in the DSP is slow, requiring over a minute to settle after the power comes on and a similar time to trip if the signal is lost, but this is sufficiently fast to detect a rare failure of a BCS component (and far better than the weekly manual testing used previously).

For the PBLM, the same microcontroller modulates the drive signal and detects the modulation; thus, the phase of self-checking tone is known and stable. For the LBLM, the modulation and detection are far apart, at the two ends of the optical fiber. The modulation and demodulation frequencies are matched by counting in firmware 75 cycles of the 60-Hz ac power line ($60/75 = 0.8$).

D. LBLM temperature and humidity

The integrated Peltier cooler in the Hamamatsu module can maintain a PMT temperature of 0 °C, to lower the dark current, only if the ambient temperature does not exceed 35 °C. On a hot summer afternoon, the temperature inside a rack in the klystron gallery of the SLAC linac may reach 50 °C. Consequently, we added an external thermoelectric cooler that transfers heat directly from the PMT housing.

To avoid condensation onto the PMT window, the external cooler is configured to operate only when the temperature of the PMT housing reaches 30 °C, which is above the dew point expected in the gallery. The chassis was tested in an environmental oven with a maximum temperature of 50 °C and a relative humidity as high as 100%. No condensation was observed on the PMT window or housing. The detected self-checking amplitude remained stable, and the input voltage offset (from the PMT dark current and electronics) remained within our requirements.

E. PBLM cables and connectors

Unlike the fiber and PMT, a diamond detector requires a bias cable to carry the high voltage from the rack outside the tunnel to the detector inside and a signal cable to carry the output current from the detector back to the rack. The signal current at the MPS threshold is small, typically a few nanoamps, and must not be shunted through the leakage resistance of the coaxial dielectric before arriving at the rack. Hence, the 15-MΩ discharge resistor in the passive *RC* filter in Fig. 10 must be well below the leakage resistance of 50–150 m of cable, a specification that manufacturers do not provide (and often do not know). Consequently, we tested long cables of different types for leakage resistance, noise immunity (good shielding), and attenuation. Double-shielded cable was preferred to avoid noise pickup from the various kicker magnets that switch the high-rate electron bunches to their various destinations.

To find the leakage resistance, each cable was charged to 500 V (which kept within its voltage specification). Then, a picoammeter with a 10-fA resolution measured the current through the dielectric. In all cases, the resistance was found to be at least 200 MΩ. The cable was then disconnected and discharged through a 50-Ω termination. Several cable types exhibited a peculiar and quite unexpected behavior: When we reconnected one end of the cable to the meter and left the other end open, the meter registered a persistent dc current of as much as 1 nA. Despite discharging for as long as a few days, the current resumed once the cable was reconnected to the meter. A voltmeter used to check the picoammeter read a consistent value of a few millivolts. Times Microwave, a cable manufacturer, suspected that friction between the dielectric and the material of the outer conductor generated the charge. They sent spools of several cable types for testing. We could not elucidate the mechanism but ultimately found that their SF-223 (a variant of RG-223) does not exhibit this persistent current.

Reynolds type C, a high-voltage cable widely used across multiple systems at SLAC, was selected for the bias. To test for pickup, the diamond and both cables were placed inside coils of large-diameter Heliax cables driving a prototype kicker in its test stand. The cables ran to the prototype diamond electronics and to an oscilloscope. No pickup was seen in the integrated detector signal.

Triaxial cable was tested with a guard drive connected to the inner braid, which held the average voltage drop at zero across the inner dielectric, to null leakage in the cable from

this braid to the center conductor. Ultimately, this was found unnecessary and, in fact, increased the leakage due to the transition from the triaxial cable to the coaxial output of the sensor.

Connectors mating with the diamond detectors are custom variants of LEMO type 00 (for bias) and SMA (for signal). The insulators use polyether ether ketone (PEEK) rather than the standard polytetrafluoroethylene (PTFE), to significantly increase the radiation tolerance.

VI. EXPERIMENTAL TESTS

A. LION and PIC versus fiber and diamond

In the experiment depicted in Fig. 12(a), a 180-pC, 5.115-GeV electron beam hit tungsten plates at 5 Hz. The loss signals were collected by several detectors placed to one side: a PIC, a short LION, two polycrystalline diamond detectors (a standard B2 and a high-radiation B4), and an optical fiber.

Figure 12(b) shows that both diamonds are faster and less noisy than the PIC. The pulse from the B4 diamond is about 5 times higher than that from the B2, although about half the width. However, the B4 is 7.5 times closer. The inverse square of the distance (an approximate correction, since the radiation field is not spherically symmetric) suggests that the B4 is less sensitive by more than a factor of 20. Ideally, an ionizing particle passing through a diamond produces 36 electron-hole pairs per micrometer of travel. The B4 is both 5 times thinner than the B2 and also intercepts fewer particles with an electrode area that is 9 times smaller. The more fractured crystal structure of the B4 also lowers the efficiency of charge collection [17].

The LION signal in Fig. 12(c), processed by standard SLAC electronics, was very slow and required a much longer timescale. It also exhibited significant 60-Hz modulation. Compare this to the fast signals in Fig. 12(d) from different photosensor types at either end of the fiber. The fiber ran along the LION, around a delay loop shielded from radiation, and back along the LION. One end had a PMT (Hamamatsu R7400U-06, a small blue-sensitive tube); the other had a silicon photomultiplier (SiPM, Hamamatsu C13360-6050CS), an array of small avalanche photodiodes that act as a solid-state PMT by combining the output of all the diodes. Ultimately, we rejected the SiPM due to its higher dark current, lower dynamic range, and cross talk between neighboring diodes. The SiPM pulse could be shortened with a transimpedance amplifier.

The upstream ends of the LION and fiber were 90° from the tungsten target, 1.5 m away. They ran downstream for 1.5 m and so ended 45° from the target in the forward direction. The large initial peaks for the PMT and SiPM signals showed the capture of forward-going light from a loss shower. The second peak, delayed by the longer path in the fiber, came from backward-going light from the shower but was not favored by the layout, since the fiber had little backward extent. Next, we present an experiment making this forward-backward comparison with a long fiber.

B. PMT location: Upstream or downstream

Cherenkov light can couple into a fiber mode traveling in either direction. Each end of the fiber offers advantages as

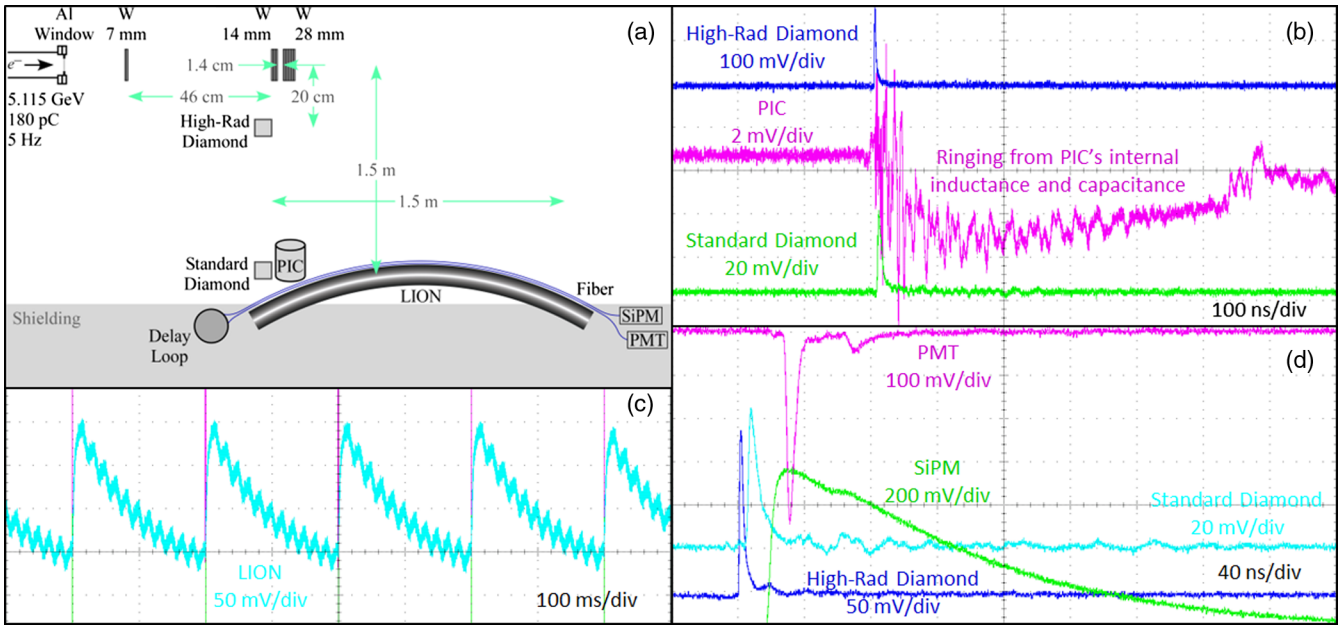

FIG. 12. (a) Layout of an experiment comparing old and new detectors as 5.1-GeV, 180-pC electron bunches hit tungsten plates. Signals from (b) a PIC and diamonds; (c) a LION, with a very slow timescale and large 60-Hz noise; and (d) a PMT and a silicon photomultiplier (SiPM).

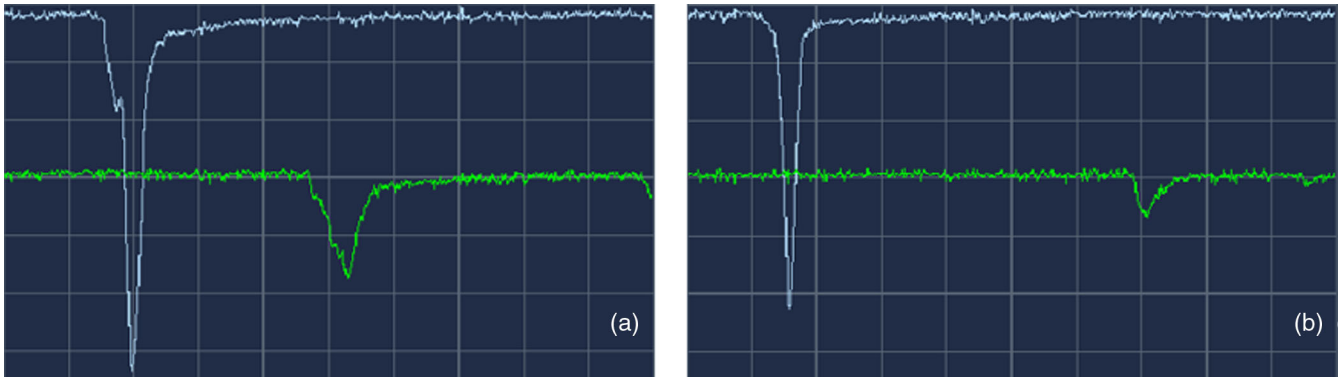

FIG. 13. Signals from PMT1 (green trace, upstream end of fiber) and PMT2 (blue, downstream end); 200 ns/div and 1 V/div into 50 Ω. The loss points are (a) 82 and (b) 39 m upstream of the beam stopper at the downstream end. As losses move downstream, the peaks move rightward for PMT1 but leftward for PMT2, and the ratio of their amplitudes PMT1/PMT2 decreases. The pulse widths and peak separations of PMT2 are compressed by 5 relative to PMT1.

the PMT location. We measured the effect with a blue-sensitive PMT (Hamamatsu R7400U-06) at each end of a 155-m fiber. The blue PMTs also allowed us to compare the measured and calculation attenuation, since the loss is higher over this distance (30 dB/km at 420 nm vs 5 dB/km at 700 nm).

Consider an electron bunch lost at z after passing the start ($z = 0$) of a fiber of length L at $t = 0$. By adding the travel times of the electrons and the light, we find that an upstream PMT (PMT1, at $z = 0$) receives its signal at $t_u(z) = (1 + n)z/c$, where the refractive index $n \approx 1.5$. The signal arrives at a downstream PMT (PMT2, at $z = L$) at $t_d(z) = (1\text{-}n)z/c + Ln/c$. Two losses a distance Δz apart produce signals separated by $\Delta t_u = (1 + n)\Delta z/c \approx 2.5\Delta z/c$ and $\Delta t_d = (1\text{-}n)\Delta z/c \approx -0.5\Delta z/c$. The signals arrive at PMT2 in reverse order and 5 times closer in time, giving PMT1 an advantage. Simply zooming in corrects for this compression until reaching a resolution limit determined by cable dispersion, PMT rise time, or digitizer bandwidth. In our case, loss localization to 3 m with a downstream PMT is achievable and sufficient.

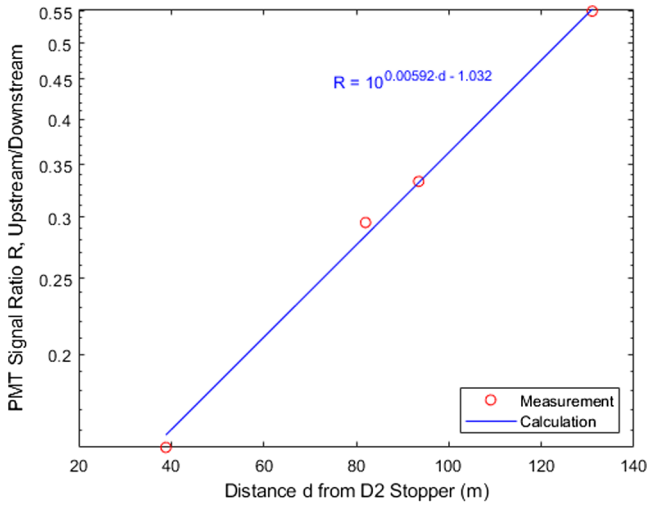

FIG. 14. PMT1/PMT2 ratio. The calculated slope comes only from the properties of the Cherenkov light, fiber, and PMT. The vertical offset, from a fit to the measurements, determined that the signal from the backward loss shower was 27% of the forward signal.

The counterargument to placing the PMT at the upstream end is that the beam-loss shower is stronger in the forward direction and so sends more Cherenkov light to a downstream PMT.

In the test, corrector magnets steered the beam into the beam pipe to generate losses at various distances from a beam stopper at the downstream end. PMT loss signals (Fig. 13) show changes in both the arrival time and amplitude. Figure 14 plots the signal ratio PMT1/PMT2. As the loss shifts downstream, the attenuation grows for PMT1 and drops for PMT2, doubling the relative attenuation. The slope of the blue line in Fig. 14 came not from a fit but from a calculation integrating over the wavelength dependence of Cherenkov emission, the fiber transmission, and the QE of this PMT. A fit to the measured points provided the offset of this line and indicated a backward-forward signal ratio of 27%. This result motivated the choice to put the PMT at the downstream end of each fiber.

C. Tails on polycrystalline diamond signals

In comparing the responses of side-by-side B1, B2, and B4 diamond detectors, we found the B2 and B4 exhibited a slow tail when the loss stopped. In Fig. 15, about 1 W of the LCLS beam was scraped on a collimator monitored by a B1 and a B2, as the beam rate was switched between 0 and 120 Hz. The polycrystalline B2 exhibited dual time constants, initially 2 s followed by 18 s, due to charge traps at domain boundaries. The B4 shows an even longer decay tail and a similarly slowed rise. The single-crystal B1 has no tails and so was chosen by the LCLS-II project for the

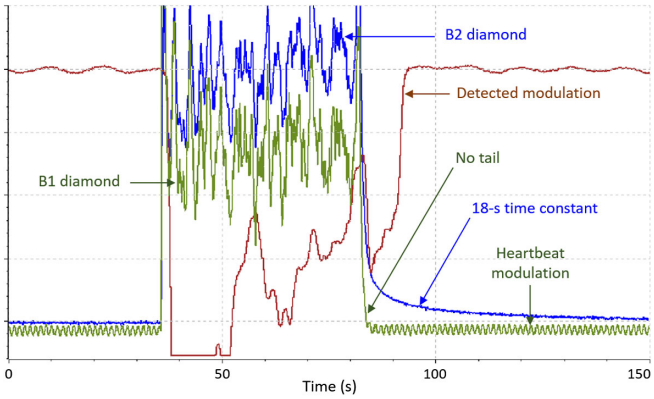

FIG. 15. Cividec single-crystal B1 (green line) and a polycrystalline B2 (blue line) detectors measure a 1-W loss on an LCLS collimator as the beam rate was toggled between 0 and 120 Hz. The B2 exhibits a long decay tail. The red signal is the heartbeat amplitude detected by the DSP.

high-rate beam. The mechanism driving these tails in the polycrystalline detectors is not well understood [17].

This experiment also gave the first opportunity to test the continuous heartbeat self-check, described earlier, in which the bias voltage is modulated at 0.8 Hz. In Fig. 15, the B1 shows a noticeable sinusoid due to a large modulation. The filter was subsequently improved, so that the lock-in now robustly detects the heartbeat from a modulation current smaller than any loss signal of interest.

D. Field emission from a cryomodule

Field emission (FE) from the niobium wall of a cryomodule originates from particulates, chemical residue, and surface imperfections [18]. The rf field pulls a small charge from an emitting site but repeats in every 1.3-GHz period. The resulting loss current can be sufficient to activate or damage the module and to produce radiation nearby. Depending on their phase at emission, FE electrons can strike a nearby wall or be accelerated and transported in either direction to other cavities or cryomodules. The LCLS NC linac is not suitable for testing the ability of the LBLM fibers to detect such losses. Instead, an experiment [19] was performed on a SC electron accelerator, CEBAF, at Thomas Jefferson National Accelerator Facility.

A 12-m fiber and two diamond detectors were tested on the last cryomodule (1L26, a C100 high-gradient type) of the CEBAF north linac. The full linac had rf power, but the photocathode laser was off, and so the only current was due to field emission from the cavities in the cryomodules. The fiber was draped along the side of the 10-m module. During the measurements in Fig. 16, a high-radiation (B4) diamond and a CEBAF beam-loss monitor (referring to a PMT with radiation-driven electron emission from the photocathode) were placed at the warm sections at either end of the cryomodule.

Figure 16(a) shows the field gradients in seven of the eight cavities of 1L26 increasing sequentially in steps of 1 MeV/m (except cavity 8, which was held constant). The other cryomodules were at full field. Two noteworthy events occurred: Cavity 7 spiked up at $t = 16$ min, and cavity 3 briefly dropped out at $t = 81$ min.

Figure 16(b) compares the loss detectors on the same time axis. The upstream BLM and diamond were dominated by losses flowing from the previous module (1L25); their signals grew weakly with the increase in gradient and barely registered the events in cavities 3and 7. The downstream BLM and diamond were at the end of the linac and so did not receive losses from a neighboring cryomodule.

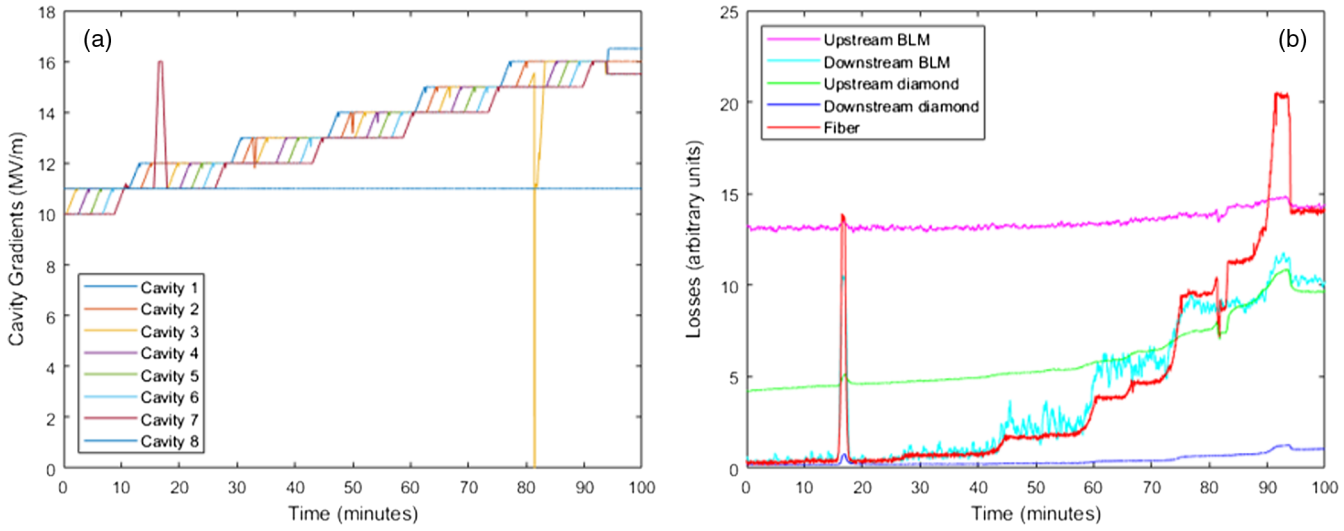

FIG. 16. (a) Gradients in the eight cavities of the cryomodule. The gradients, except in cavity 8, were stepped sequentially by 1 MV/m. Cavity 7 had an upward spike at $t = 16$. Cavity 3 briefly dropped out at $t = 81$. (b) Losses from field emission picked up by five detectors. Only the fiber was sensitive to the sudden changes in both cavities 3 and 7.

They showed the rf-gradient steps, although with noise (BLM) or a weak response (B4). They responded to the nearby event, in cavity 7, but did not see the drop-out in cavity 3.

The fiber responded only to 1L26 and was highly sensitive to losses from its interior cavities. It showed strong growth in field emission with each step in cavity 7, especially at the highest gradients, and jumped up with that cavity's upward spike. It decreased, but less sharply, for the drop-out of cavity 3, indicating that the total signal was dominated by cavity 7. The last upward step of cavity 7, at $t = 91$, caused a large jump in the fiber signal, and the subsequent gradient reduction by 0.5 MV/m, at $t = 94$, reduced the loss signal sharply. We see that the fiber is sensitive to this level of field emission. The source can be located by scanning cavity gradients.

The cryomodules of the LCLS SC linac are welded together, without intervening warm sections (except at the bunch compressors), which at CEBAF provide periodic access for loss detectors. A fiber parallel to the beam just outside the cryomodules provides a sensitive alternative.

E. Wire scanner

Previously, LCLS used dedicated, large-cross-section plastic fibers to detect losses during wire scans. Such fibers are known to blacken with radiation and so are unsuited for use with the SC linac. Moreover, it is inefficient to introduce additional fibers, PMTs, and integrating electronics if a good bunch profile can be obtained by sharing the diagnostic output of the new fibers. A 100-m length of the new fiber was installed 1.25 m from the LCLS NC beam, beginning at a wire scanner. Figure 17 shows a test of a wire scan made using this new fiber, an uncooled PMT, and the old LCLS wire-scanner electronics.

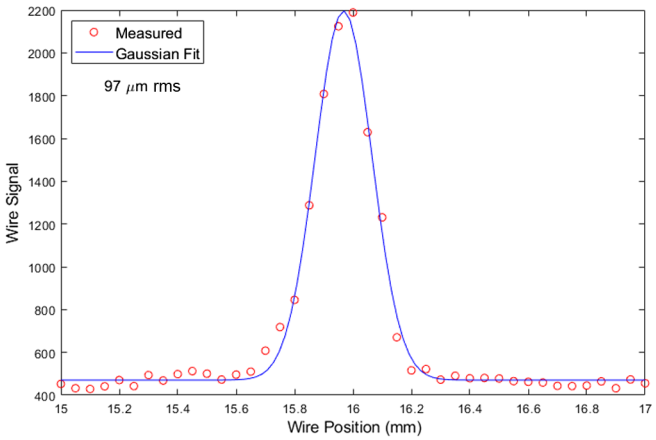

FIG. 17. Wire scan of the LCLS vertical beam profile during tests of the quartz fiber.

VII. SUMMARY

The LCLS-II project at SLAC adds a new superconducting linac and replaces the original undulator of the x-ray FEL with two new undulators, for hard and soft x rays. The SC linac, now being installed, will have continuous rf, a bunch rate of up to 1 MHz, and up to 120 kW of beam power. This motivated a reexamination of beam-loss detection and protection systems. The previous loss monitors, based on ionization chambers, have the potential to become nonlinear at high loss rates.

Newer technologies have been selected. Key points of concern for beam loss will be protected locally with diamond detectors, which act as solid-state ionization detectors making electron-hole pairs. The entire length of the machine will be spanned in segments by radiation-hard optical fibers. A loss shower emits Cherenkov radiation when passing through the fiber; this light is transmitted to a PMT at one end. Both detector types will be continuously tested by a low-level modulation at 0.8 Hz.

Both detector types have been subjected to extensive testing to qualify them as components in critical safety systems for protection of personnel, radiation safety equipment, the accelerator, and the beam lines.

ACKNOWLEDGMENT

This work was supported by the U.S. Department of Energy, Office of Science, under Contract No. DE-AC02-76SF00515.

[1] P. Emma *et al.*, First lasing and operation of an ångstrom-wavelength free-electron laser, Nat. Photonics **4**, 641 (2010).
[2] LCLS-II final design report, SLAC Report No. LCLSII-1.1-DR-0251-R0, 2015.
[3] V. Yakimenko *et al.*, FACET-II facility for advanced accelerator experimental tests, Phys. Rev. Accel. Beams **22**, 101301 (2019).
[4] J. J. Welch, Radiation detection requirements for the BCS and MPS, LCLS-II physics requirements document, SLAC Report No. LCLSII-2.4-PR-0868-R1, 2018.
[5] T. N. Constant, R. W. Zdarko, R. W. Simmons, and B. M. Bennett, LIONs at the Stanford Linear Accelerator Center, SLAC Report No. SLAC-PUB-7691, 1998.
[6] R. M. Zwaska *et al.*, Beam tests of ionization chambers for the NuMI neutrino beam, IEEE Trans. Nucl. Sci. **50**, 1129 (2003).
[7] M. Santana Leitner, Fluence to dose conversion E-curves for silicon and polyethylene. A FLUKA user-routine to convert fluence into energy deposition in small radiation sensitive accelerator components, SLAC radiation physics Note No. RP-14-20, example 3, doses near a stopper.
[8] I. Dumanoglu *et al.*, Radiation-hardness studies of high OH^- content quartz fibres irradiated with 500-MeV electrons, Nucl. Instrum. Methods Phys. Res., Sect. A **490**, 444 (2002).

[9] K. Cankoçak, M. N. Bakırcı, S. Çerçi, E. Gülmez, J. P. Merlo, Y. Onel, F. Özok, I. Schmidt, and N. Sönmez, Radiation-hardness measurements of high OH^- content quartz fibres irradiated with 24-GeV protons up to 1.25 Grad, Nucl. Instrum. Methods Phys. Res., Sect. A **585**, 20 (2008).

[10] P. G. Bruecken *et al.*, Results from post situ quartz fiber neutron irradiations, CMS Internal Note No. CMS-IN-2006/000, 2006.

[11] J. D. Jackson, *Classical Electrodynamics*, 3rd ed. (John Wiley and Sons, New York, 1999), Sec. 13.4.

[12] http://photocool.com/tocool.htm.

[13] M. Santana-Leitner *et al.*, Monte Carlo optimization of fast beam loss monitors for LCLS-II, in *Proceedings of the International Particle Accelerator Conference (IPAC'19), Melbourne, Australia* (JACoW Publishing, Geneva, Switzerland, 2019), THPRB102, pp. 4066–4069, https://doi.org/10.18429/JACoW-IPAC2019-THPRB102.

[14] https://cividec.at/.

[15] C. Weiss, M. Cerv, E. Griesmayer, and P. Kavrigin, Particle interactions with diamond detectors, in *Proceedings of the International Beam Instrumentation Conference (IBIC'19), Malmö, Sweden* (JACoW Publishing, Geneva, Switzerland, 2019), pp. 115–117, MOPP016, https://doi.org/10.18429/JACoW-IBIC2019-MOPP016.

[16] R. Kadyrov *et al.*, Electronics for LCLS-II beam containment system loss monitors, in *Proceedings of the International Conference on Accelerator and Large Experimental Physics Control Systems (ICALEPCS'19), New York, NY* (JACoW Publishing, Geneva, Switzerland, 2019), THCPR07, http://icalepcs2019.vrws.de/papers/thcpr07.pdf.

[17] E. Griesmayer, Cividec Instrumentation (private communication).

[18] R. L. Geng, A. Freyberger, R. Legg, R. Suleiman, and A. S. Fisher, Field emission in SRF accelerators: Instrumented measurements for its understanding and mitigation, in *Proceedings of the International Beam Instrumentation Conference (IBIC'17), Grand Rapids, MI* (JACoW Publishing, Geneva, Switzerland, 2017), TH1AB1, pp. 470–477, https://doi.org/10.18429/JACoW-IBIC2017-TH1AB1.

[19] A. S. Fisher *et al.*, Beam containment and machine protection for LCLS-2, in *Proceedings of the International Beam Instrumentation Conference (IBIC'17), Grand Rapids, MI* (JACoW Publishing, Geneva, Switzerland, 2017), pp. 478–481, TH1AB2, https://doi.org/10.18429/JACoW-IBIC2017-TH1AB2.